Characterisation and evaluation of a PNP strip detector for synchrotron microbeam radiation therapy

Jeremy A. Davis
University of Wollongong, jeremyd@uow.edu.au

Jason Paino
University of Wollongong, jrp933@uowmail.edu.au

Andrew Dipuglia
University of Wollongong, ad150@uowmail.edu.au

Matthew Cameron
University of Wollongong, mc815@uowmail.edu.au

Rainer Siegele
Australian Nuclear Science And Technology Organisation

See next page for additional authors

Recommended Citation

Characterisation and evaluation of a PNP strip detector for synchrotron microbeam radiation therapy

Abstract

The Quality Assurance requirements of detectors for Synchrotron Micro-beam Radiation Therapy are such that there are limited commercial systems available. The high intensity and spatial fractionation of synchrotron microbeams requires detectors be radiation hard and capable of measuring high dose gradients with high spatial resolution sensitivity. Silicon single strip detectors are a promising candidate for such applications. The PNP strip detector is an alternative design of an already proven technology and is assessed on its contextual viability. In this study, the electrical and charge collection efficiency properties of the device are characterised. In addition, a dedicated TCAD model is used to support ion beam induced charge measurements to determine the spatial resolution of the detector. Lastly, the detector was used to measure the full width half maximum and peak to valley dose ratio for microbeams with only a slight over response. With the exception of radiation hardness the PNP detector is a promising candidate for quality assurance in microbeam radiation therapy.

Disciplines

Medicine and Health Sciences

Publication Details

Authors

Jeremy A. Davis, Jason Paino, Andrew Dipuglia, Matthew Cameron, Rainer Siegele, Zeljko Pastuovic, Marco Petasecca, Vladimir Perevertaylo, Anatoly B. Rosenfeld, and Michael L. F Lerch

Characterisation and Evaluation of a PNP Strip Detector for Synchrotron Microbeam Radiation Therapy

Jeremy A. Davis[1,2], Jason R. Paino[1], Andrew Dipuglia[1], Matthew Cameron[1], Rainer Siegele[3], Zeljko Pastuovic[3], Marco Petasecca[1,2], Vladimir L. Perevertaylo[4], Anatoly B. Rosenfeld[1,2], Michael L. F. Lerch[1,2]

[1]Centre for Medical Radiation Physics, University of Wollongong, Wollongong, N.S.W., Australia
[2]Illawarra Health and Medical Research Institute, University of Wollongong, Wollongong, N.S.W., Australia
[3]Centre for Accelerator Science, Australian Nuclear Science and Technology Organisation, Lucas Heights, AUS
[4] SPA-BIT, Kiev, Ukraine

E-mail: `jeremyd@uow.edu.au`

Abstract. The Quality Assurance requirements of detectors for Synchrotron Microbeam Radiation Therapy are such that there are limited commercial systems available. The high intensity and spatial fractionation of synchrotron microbeams requires detectors be radiation hard and capable of measuring high dose gradients with high spatial resolution sensitivity. Silicon single strip detectors are a promising candidate for such applications. The PNP strip detector is an alternative design of an already proven technology and is assessed on its contextual viability. In this study, the electrical and charge collection efficiency properties of the device are characterised. In addition, a dedicated TCAD model is used to support ion beam induced charge measurements to determine the spatial resolution of the detector. Lastly, the detector was used to measure the full width half maximum and peak to valley dose ratio for microbeams with only a slight over response. With the exception of radiation hardness the PNP detector is a promising candidate for quality assurance in microbeam radiation therapy.

PACS numbers: 00.00, 20.00, 42.10

Keywords: Microbeam Radiation Therapy, Dosimetry, Quality Assurance

1. Introduction

Synchrotron Microbeam Radiation Therapy (MRT) is a next generation radiotherapy modality that takes advantage of the comparable tolerance of healthy tissue over cancerous tissue to high doses of spatially fractionated X-rays, i.e. Dose-Volume effect

[1], [2]. The low beam divergence and brilliance of synchrotron radiation allow for high dose rates (20 kGy s^{-1}) to minimise any dose blurring effects associated with cardiosynchronous movement of the target. MRT is currently in the preclinical phase, with testing restricted to small animals. Studies have shown the effectiveness of MRT in decreasing tumour size and/or ablating tumours completely as well as increased survival rates in tumour-bearing rodents [3], [4] [5], [6].

Synchrotron radiation at the Australian Synchrotron (AS) is produced by 3 GeV electrons circulating in an evacuated storage ring with diameter of 216 m. Unlike many other synchrotron facilities, the AS runs in continuous 'top-up' mode allowing for a relatively constant electron current in the beam line at all times, foregoing the need for any correction in measured parameters that vary with a time variant current. For the purpose of MRT, synchrotron radiation produced in the 'wiggler' field exits the storage ring onto the Imaging and Medical Beam Line (IMBL). The synchrotron radiation beam is then passed through various filters to appropriately moderate the beam for specific applications, i.e. imaging and therapy. The energy of the resultant x-ray energy spectrum will vary between 40-600 keV, with a mean energy (depending upon the wiggler field and filtration) typically between 60-500 keV [7]. Fractionation of the radiation field, typically centimeters wide and millimeters high is achieved through the insertion of a custom tungsten Multi Slit Collimator (MSC) into the synchrotron X-ray beam approximately 1 m upstream of the target. The result is an array of quasi parallel x-ray micro-beams with width between 25-75 µm and pitch of 200-400 µm depending on the specific geometry of the MSC [8].

It is clear that within the context of Quality Assurance (QA), that the same methods and detectors used in more traditional radiotherapy treatments are not applicable for MRT. The beam structure alone makes QA an incredibly complex and challenging task. The possibility of deviations in the synchrotron beam and movement artefacts add to these challenges which we are attempting to address through online real time dosimetry. The Full Width Half Maximum (FWHM) of the micro-beams is an important parameter used to assess the quality of the MRT field. Accurate measurement of FWHM of each microbeam demands a detector with micron scale spatial resolution [9]. The microbeam pitch is typically much greater than the FHWM of the microbeam peak however significant dose can be delivered to the regions between the microbeams and is referred to as the valley dose. The use of beam moderators/filters is optimised to deliver the required high dose within the peak whilst maintaining valley doses to be within the normal tissue tolerance. A quantitative measure of this can be determined through measurement of the Peak to Valley Dose Ratio (PVDR). The absolute dose at any particular depth will vary depending upon the position within the profile of the microbeam field, i.e. within a peak or valley of the micro-beam array, and can vary from a fraction of a Gy to tens or even hundreds of Gy. It is therefore necessary that detectors be radiation hard and capable of measuring accurately over a large dynamic range of radiation dose. At present there is no commercial system available that is suitable for this task under all MRT irradiation field sizes. It is therefore necessary to

develop devices that can meet the needs of this emerging cancer treatment. At present, there are a number of technologies that are being utilised in MRT facilities, although each has its shortcomings and even when used in concert, fail to address the criteria previously mentioned. To date, the most successful technologies are Gafchromic film [10], Samarium-Doped Oxyfluoride Glass-Ceramics [11] [12], the PTW microdiamond [13] [14] and the 50 µm Single Strip Detector (SSD) produced by Centre for Medical Radiation Physics (CMRP) [9] [15]. Whilst Gafchromic film is able to satisfy many of the necessary criteria previously stated, it suffers from the long development time required to measure dose accurately, limiting its use to scenarios where a significant delay between exposure and quantitative measurement data is tolerable. This limits the use of Gafchromic film to purely support/reference measurements. Like Gafchromic film, Samarium-Doped Oxyfluoride Glass-Ceramics have the potential to satisfy many of the requirements of a reference dosimeter for MRT applications having the potential to measure both FWHM and PVDR [11] [12]. Unlike Gafchromic film, these novel materials have the additional advantage of being reusable, given suitable high temperature heat treatment or UV exposure. Unfortunately, due to the requirement of confocal microscopy to provide a measure of the synchrotron x-ray induced photoluminescent signal, they cannot currently be used in real time dosimetry. The PTW microdiamond, satisfies the online requirement but requires significant settling time (the order of 1 second) for precise measurements leading to long data acquisition times when performing high spatial resolution (e.g. 0.005 mm step size) profile measurements. Whilst it has the required spatial resolution, it is dependent upon a rigorous and time consuming alignment methodology, making it less ideal for clinical applications. The 50 µm Single Strip Detector (SSD) designed at CMRP and fabricated at SPA-BIT, Kiev, Ukraine has been previously shown to be a promising candidate. It has successfully measured FWHM and PVDR of microbeams in real time, making it ideal as an dosimetric analysis tool [15]. However, in order to achieve the necessary spatial resolution for microbeam profiling the device must be operated in edge-on mode which may lead to measured profile artefacts [16] [17]. These issues are linked to the design and fabrication process which have been addressed in later prototypes such as the PNP detector. In this paper, an alternative prototype of the SSD previously discussed is examined and evaluated with respect to applicability for QA in MRT. Full details related to the electrical and charge collection characteristics will be presented. This will be supported by a dedicated Synopsys TCAD simulation. In addition, the performance of the detector for synchrotron microbeams is also shown.

2. Detector Specifics

The PNP device was designed at CMRP and fabricated at SPA BIT, Kiev, Ukraine. In contrast with previous single strip detectors (SSD) [9], [15], [18], the 'PNP' device is fabricated entirely within n-type epitaxial silicon. The diode structure was fabricated by means of ion implantation within 7 µm thick 100 Ω cm n-type silicon upon a 300 µm low

resistivity (0.001 Ω cm) substrate. The single strip (p+) of dimensions 500 x 5 µm^2 is surrounded by an n-type ground ring (width and separation = 5 µm) and p-type guard ring (width and separation = 5 µm) respectively, see Fig. 1. In this design we attempted to overcome the need for using the strip detector in edge-on mode (necessitated by limitations in the processing technique related to feature size) by incorporating an additional exterior diode ring. It was envisaged that by having a smaller bias voltage on the inner strip diode relative to the outer ring diode we could improve the effective spatial resolution of the device when used in face-on mode. A layer of SiO$_2$ surrounds the diode structure in order to protect the device from unwanted contaminants and reduce surface leakage currents. Throughout this work, the PNP devices were mounted upon two different types of packages. For the purpose of electrical and charge collection characterisation, the PNP device was mounted upon a standard 20 pin dual in-line package, whilst for experiments at the AS, the PNP device has been mounted upon a purpose-made 600 µm thick, 10 mm wide and 300 mm long kapton probe as described by Petasecca, et al, 2012. This flexible 'Drop-In' technology minimises dose enhancement that is common with commercial components. It also allows for use within both solid and liquid water phantoms, making it ideal for QA [9].
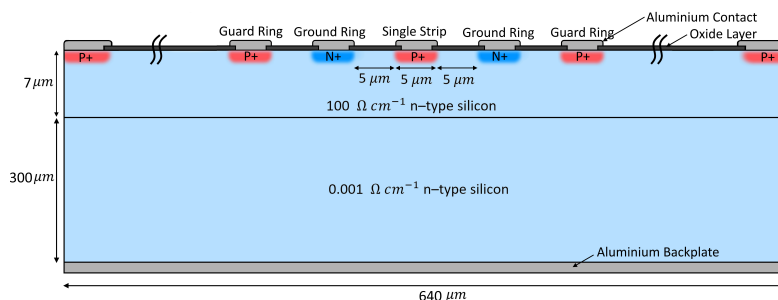

Figure 1. Cross-section diagram of the PNP device. Wavy lines indicate a discontinuity for scaling purposes.

3. Method

3.1. Electrical Characterisation

The primary aims of characterising the electrical performance of the PNP SSD is to first determine its functionality and then secondly ascertain the level of leakage current and noise inherent to the system. Following basic diode testing to ensure the device was in working order, Current-voltage (I-V) measurements of the PNP were undertaken using a Keithley 6517A electrometer. Measurements were undertaken with reverse bias (-50<V<0) applied to the strip and the back contact connected to a virtual ground, corresponding to an input of electrometer. A 1 s delay between each step was implemented in order to allow measured currents to stabilise. A current threshold of 0.5 µA was imposed in order to protect the devices from overload. Capacitance-voltage
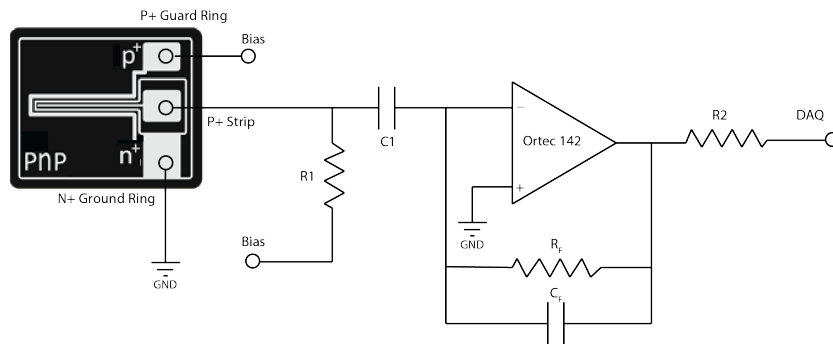
Figure 2. Simplified circuit schematic for IBIC measurements

(C-V) measurements were performed upon a Boonton capacitance meter (Model 7200) controlled by a PC via an IEEE-488 interface. The system was calibrated prior to testing without the device connected to cancel out capacitance contributions inherent in the experimental set-up. The Boonton 7200 provides fast characterisation of components at 1 MHz, and has a resolution of 0.01 pF with a measurement error of 0.5%. It utilises two phase sensitive detectors to perform simultaneous measurements of the device capacitance under a known bias and frequency, in order to produce a capacitance value in pF. As with the I-V measurements previously described, all C-V measurements are performed with a 1 s delay between voltage steps for the purpose of measurement stability.

3.2. Characterisation of Charge Collection Efficiency

The Ion beam induced charge (IBIC) microscopy [19] [20] measurements in different biasing conditions were performed on the PNP detector in order to determine its radiation detection properties and the spatial dimensions of the sensitive volume (SV) of the strip. Since the PNP SSD is reliant upon surrounding guard rings to limit the collection of charge from outside the SV, such studies are crucial in order to evaluate the fabrication technology with respect to the definition and thus spatial resolution of the SV. The IBIC microscopy of the PNP SDD was performed at the new SIRIUS microprobe facility at the Australian Nuclear Science and Technology Organisation (ANSTO) [21]. In this study, 5.5 MeV He^{2+} ions, having an approximate range of 28.02 μm in Silicon [22] were made incident upon the PNP surface. The ion microbeam with a spot size of approximately 500 nm x 1000 nm (X,Y) was rapidly raster-scanned at normal incidence to the sample surface. Scanned regions of interest were divided into a map of 256 by 256 pixels, with a pixel dwell time of 500 microseconds. The microbeam particle rate of 1000 +/- 100 ion/s was maintained during IBIC microscopy measurements such that individual ion impacts could be acquired consistent with the time constant of the data acquisition system [19].

A negative bias was applied to both the strip and guard ring electrodes, whilst

ground ring electrode was connected to a virtual ground, see Fig. 2. The signal due to induced current by moving charge carriers to biased collecting strip electrode following the impact of each ion projectile was integrated using a charge sensitive pre-amplifier (Ortec 142), amplified using a shaping amplifier, sorted using a multi-channel analyser (MCA) and recorded by a dedicated data acquisition system (DAQ). The generated signal has an amplitude equivalent to the ionisation energy induced by each ion impact. The signal corresponding to each energy deposition (edep) event is recorded in coincidence with beam position (x,y) to form data triplets (x, y, edep). Energy calibration is performed using a pulse generator calibrated to the response of 5.5 MeV He^{2+} ions within a 300 µm thick windowless Hammamatsu silicon PIN diode with known CCE of 100%.

The data is plotted as MCA spectra and median energy maps using custom scripts written in Matlab. Median energy maps undergo further processing in order to eliminate dark pixels, the map resolution was down-sampled to 128 by 128 pixels taking the median of 4 pulse heights. The data was then up-sampled back to a 256 by 256 map using cubic splining to retain initial pixel numbers. The data was then passed through a median filter to further reduce noise.

3.3. TCAD Modelling

The PNP SSD was modelled using Synopsys Technology Computer Aided Design (TCAD) software [23]. A 2D model of the PNP device was designed to represent a cross-section of the device, taken through the center of the strip. The model was designed to include all of the relevant/pertinent features i.e., guard and ground rings, strip contacts and polarising contacts. A box method meshing strategy was utilised in this study. In order to balance computational time and accuracy of calculations, the number of meshing elements was restricted to approximately 30,000. The meshing strategy was optimised such that finer mesh elements were applied to regions of interest. The model makes use of the Device Simulation for Smart Integrated Systems (DESSIS) code which is part of Synopsys TCAD package. The DESSIS toolkit solves the transient Poisson equation and electron and hole continuity equations for the PNP device. The model implemented includes essential models to describe the physics of the charge transportation and ion interaction within the device. The doping dependent Shockley-ReadHall physics model was employed to describe carrier generation and recombination in terms of the appropriate carrier continuity equations. The mobility model specified was utilized to take into account carrier scattering via ionised impurities, saturation of carrier velocity in regions of high electric fields and the potential for mobility degradation due to scattering driven by surface roughness. The effects of trapping and associate charge recombination at oxide interfaces were considered in this model. Given that the devices had not been exposed to radiation prior to experimentations listed in this work, only traps within the Si/SiO$_2$ interface layer were detailed. A fixed charge constant concentration of 5x10^{10} was instantiated for all Si/SiO$_2$ interfaces.

Parameter	Value
Electron energy in storage ring	3.032 GeV
Storage ring current	200.2 mA
Peak magnetic field	3.2 T
Clean up slits aperture	1 mm x 1 mm
Beam Defining Aperture	30 mm x 2.015 mm
Distance from the source	32 m
Filtration in hutch 1A	+ 10 mm C at 45° (Eq. thickness = 14.14 mm)
	+ 2 mm Cu at 45° (Eq. thickness = 2.83 mm)
Filtration in hutch 1B	0.35 mm Be
Ex-Vacuo Filtration*	4.65 mm Cu

Table 1. Parameters used for the calculation in G4-IMBL. *Ex-Vacuo filtration is used only when specified.

The purpose of this model was to evaluate the performance of the device with respect to electric field distribution under experimental conditions.

3.4. Synchrotron Testing

Microbeam experiments were performed upon the Imaging and Medical Beam Line (IMBL) at the Australian Synchrotron (AS) in Hutch 2B. Hutch 2B is positioned 32 m away from the wiggler source. A beam-defining aperture with width 30 mm and height 2.015 mm was used to define the beam dimensions. A Gammex solid water polymer phantom was scanned vertically through the beam at a scan speed of $2 \, \text{mm} \, \text{s}^{-1}$. Vertical microbeams with peak width of 50 µm and a peak-to-peak distance or pitch of 400 µm are created with the insertion of custom tungsten MSC.

All measurements are performed at 20 mm depth within the aforementioned Gammex solid water phantom which has been shown to be acceptable for use in MRT [24]. Measurements are performed with/without ex-vacuo filtration when specified. The energy spectra was calculated using SPEC [7] with the parameters provided in Table 1 which has been validated to model the AS-IMBL. This was used to assess the affect of filtration upon the energy spectra. The effect of this additional filtration is a hardening of the synchrotron radiation shifting the peak energy from 93 keV (without ex-vacuo) to 104 keV (with ex-vacuo). PNP measurements are performed in both face-on and edge-on mode, where face-on mode is hereafter defined as the beam being normally incident with respect to the surace of the PNP device, whilst edge-on mode is with the device rotated by 90° with respect to the beam direction. All measurements obtained with the PNP device were performed at a bias of -2 V, applied to the strip contact with the guard ring left 'floating'. The dosimetric response of the PNP device is calibrated with respect to a PTW PinPoint 31014 ionisation chamber (IC) [13]. The PNP devices performance will be based upon its measurements of the FWHM, PVDR and peak-to-peak distance

of the microbeams.

4. Results

4.1. Electrical Characterisation

The results derived from current-voltage tests are presented in Fig. 3. The I-V characteristics are typical of silicon diodes and remain fairly consistent between the two devices tested. The I-V plot provides a basis in which to determined the optimal bias range for device operation. The leakage current of the device below -10 V is less than 0.001 nA. The low leakage current implies that the PNP device should be capable of a high signal-to-noise ratio. Further inspection shows that breakdown voltage occurs at approximately -52 V and -55 V.
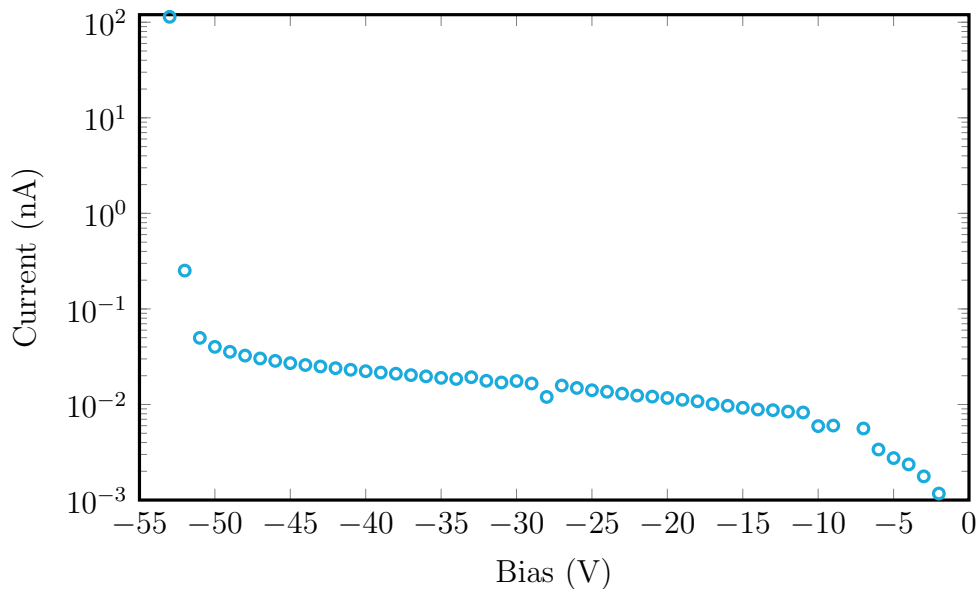
Figure 3. I-V Characteristics of the PNP detector

The capacitance-voltage measurements presented in Fig. 4 indicate that full depletion is achieved at very low bias operation. The low capacitance (pF) over the bias range tested ($0 \leq V \leq -20$) show that the PNP devices are capable of the low noise operation required for effective QA applications for dosimetry in radiotherapy treatments like MRT. If the bias is increased however a second feature becomes apparent. This additional component is hypothesised to be the result of the penetration of the electric field through the silicon dioxide surface layer underneath the contact region, leading towards a change in the overall capacitance of the PNP device. Evidence in support of this hypothesis will be presented in the next section related to charge collection characterisation.
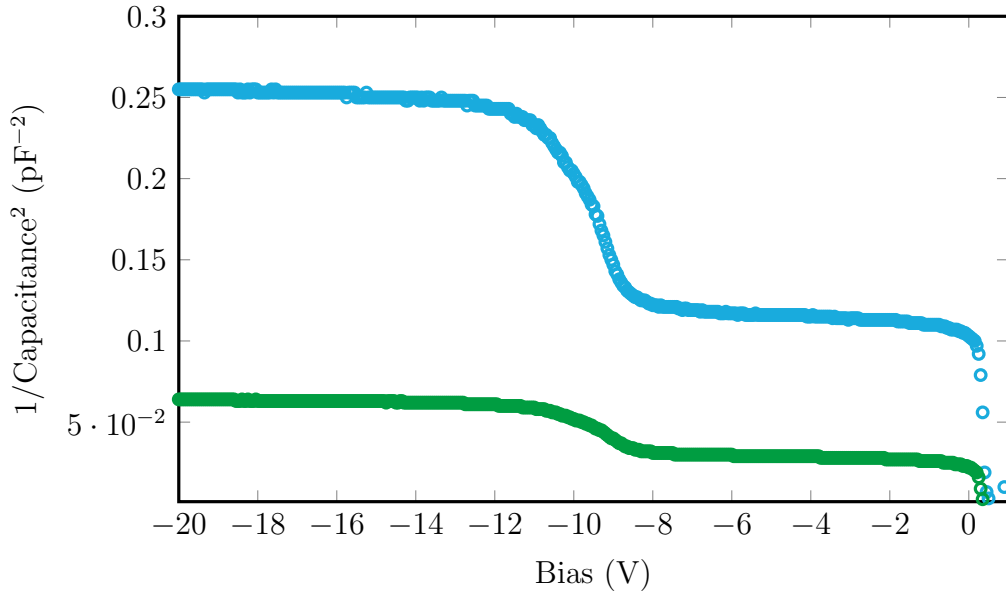
Figure 4. C-V Characteristics of the PNP detector with guard ring floating (blue markers) and biased at -2 V (green markers).
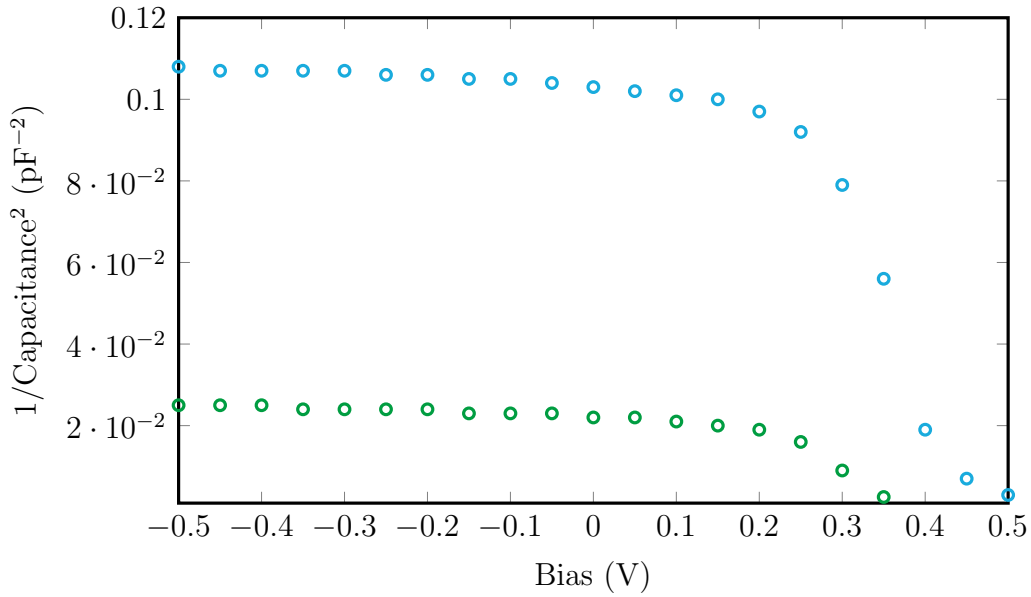

Figure 5. Zoomed in plot of the C-V Characteristics of the PNP detector with guard ring floating (blue markers) and biased at -2 V (green markers).

Analysis of the capacitance voltage measurements (see Fig. 5) can be performed using the classical formulation of a one sided abrupt junction, as detailed in Equation 1 Where C is the capacitance, q_e the charge of an electron, $\varepsilon_S = \varepsilon_o \times \varepsilon_r$, where ε_o and ε_r are the permittivity of free space and silicon respectively, N is the impurity concentration, A is the effective diode area , V the applied voltage, and ϕ_i the built-in potential

of the junction. This allows for an approximate determination of relevant quantities based upon the assumption that the PNP device can be describe as behaving like a one sided junction, i.e., built-in potential, doping concentration and depletion length, that are specific to the PNP device.

$$\frac{1}{C^2} = \frac{2}{q_e \varepsilon_s A^2 N} \left(\phi_i - V \right) \tag{1}$$

The built-in potential (ϕ_i) of the junction of the PNP device with the guard ring connected can be determined by extrapolating the gradient within the linear region such that there is an intersection of the ($1/C^2$) line with the horizontal axis, which for the presented results is approximately 0.43 V. Using Equation 2, the impurity concentration of the PNP device is estimated to be approximately 4.1 $\times 10^{15}$ cm^{-3}.

$$\frac{d\frac{1}{C^2}}{dV} = -\frac{2}{q_e \varepsilon_s A^2 N} \tag{2}$$

Lastly, using the full depletion approximation of a metal-semiconductor junction for n-type material (Equation 3), the depletion width at -2 V can be determined to be 0.87 µm.

$$W = \sqrt{\frac{2\varepsilon_s(\phi_i - V)}{q_e N}} \tag{3}$$

4.2. Ion Beam Induced Charge Measurements

IBIC measurements were performed with the strip of the PNP device under an a variety of bias conditions for detection of 5.5 MeV alpha particles. The Bragg peak which described the energy loss of the 5.5 MeV alpha particle i.e. energy deposition per micron versus depth, as determined by SRIM [22]. The range of the 5.5 MeV alpha particle is approximately 28.02 µm and thus most of the energy deposition will not be within the 7 µm thick sensitive layer. The maximum energy deposition was determined by a windowed integration of the data to 7 µm, which is approximately 0.989 MeV [22].
In this work, the 'ground' ring was grounded at 0, whilst the guard ring was either biased at 0, -2 and -5 V. The MCA spectrum and median energy map corresponding to these measurements is presented in Fig. 6, 7 and 8 respectively. The primary peak visible in the MCA spectrum corresponds to charge collection of approximately 0.8 MeV within the strip and guard ring at 0 V. This corresponds to a charge collection efficiency (CCE) of almost 81 %. The results of IBIC measurements demonstrate that the PNP architecture is effective at isolating charge collection to the strip or sensitive volume (SV) region with the width of the SV region.

However, if the bias of the strip and guard ring is increased to -10 and -20 V, charge collection is no longer restricted to the strip, and the contact pad begins to contribute significantly to the overall signal. This is evident in Fig. 9 and 10, where a second
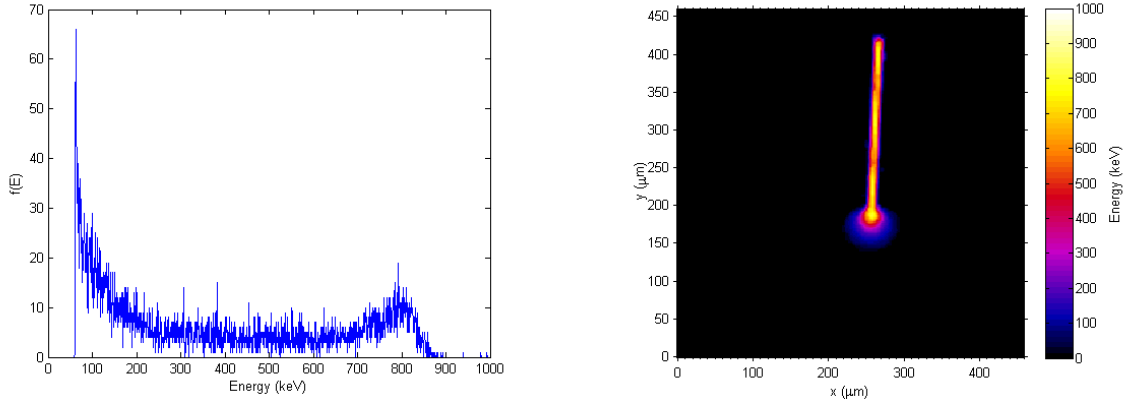
Figure 6. IBIC results for PNP detector with strip and guard ring biased at 0 V. MCA spectra (left) and median energy map (right).
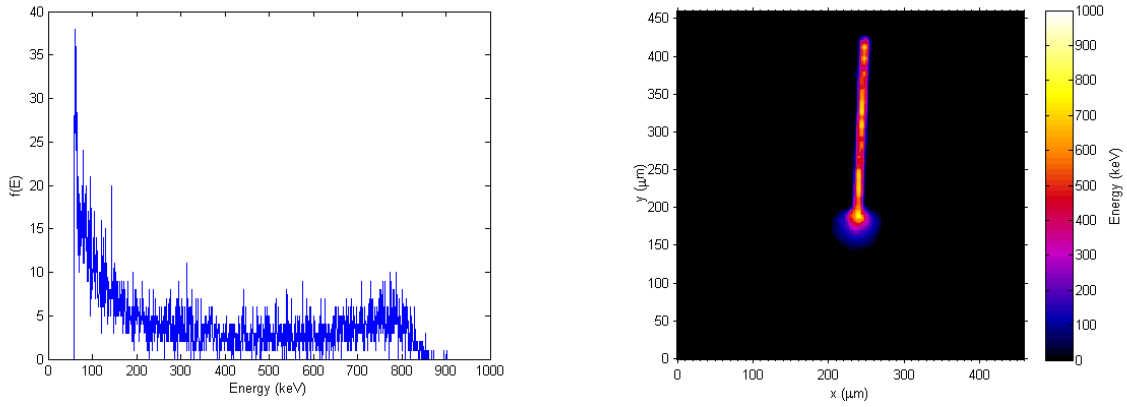

Figure 7. IBIC results for PNP detector with strip and guard ring biased at -2 V. MCA spectra (left) and median energy map (right).
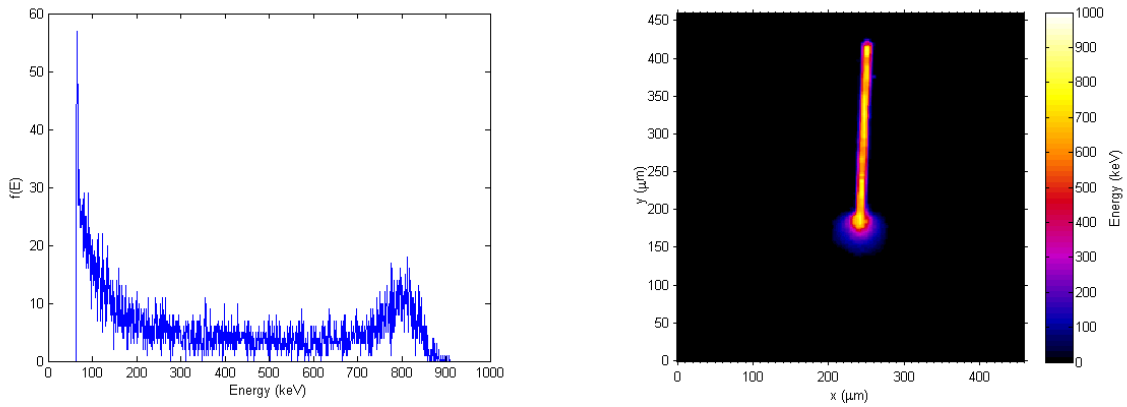

Figure 8. IBIC results for PNP detector with strip and guard ring biased at -5 V. MCA spectra (left) and median energy map (right).

peak at 0.38 and 0.62 MeV in the MCA spectrum for -10 and -20V respectively. This feature arrives from the expansion of the electric field beneath the contact and through

the silicon dioxide layer and thus extension of the depletion region which is also evident in the capacitance-voltage measurements previously discussed (see Fig. 4).
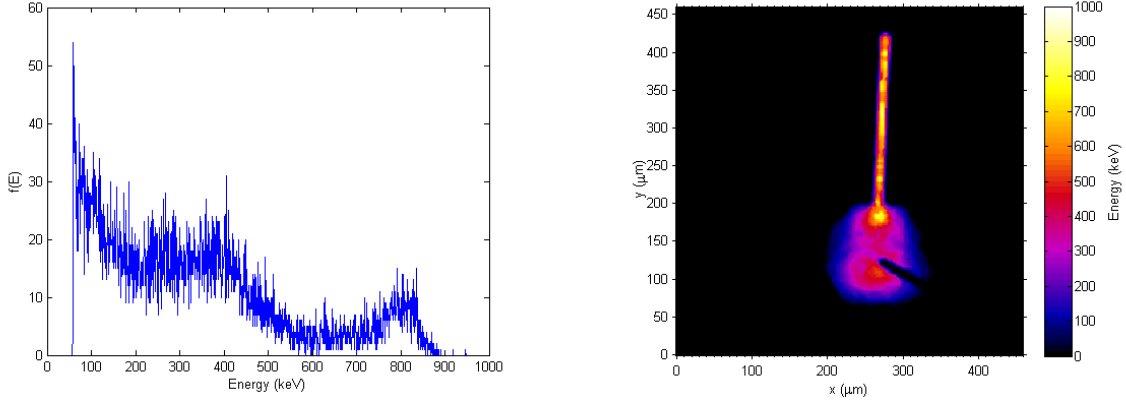

Figure 9. IBIC results for PNP detector with strip and guard ring biased at -10 V. MCA spectra (left) and median energy map (right).
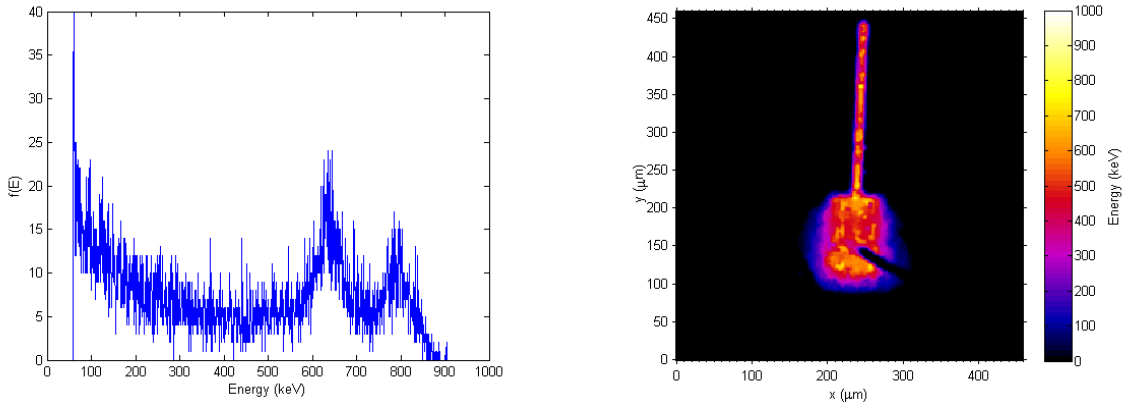

Figure 10. IBIC results for PNP detector with strip and guard ring biased at -20 V. MCA spectra (left) and median energy map (right).

The confinement of charge collection to the strip region is illustrated in Fig. 11. The median energy maps from Fig. 7 and 9, have been rotated and over-layed onto an optically zoomed microscopy image of the PNP detector. This result provides a demonstrably clear impact of bias configuration as related to the spatial resolution of the device. As the bias increases to -10V, the spatial resolution in this face-on mode operation is no longer defined by the strip. Instead, the contribution from underneath the contact region become significant leading to a undesirable degradation of the spatial resolution of the PNP detector.

This experiment was also used to examine the effect of bias upon the definition of the sensitive volume of the strip. This was achieved by applying a constant bias (-2 V) to the strip, whilst varying the bias applied to the guard ring. This result is depicted
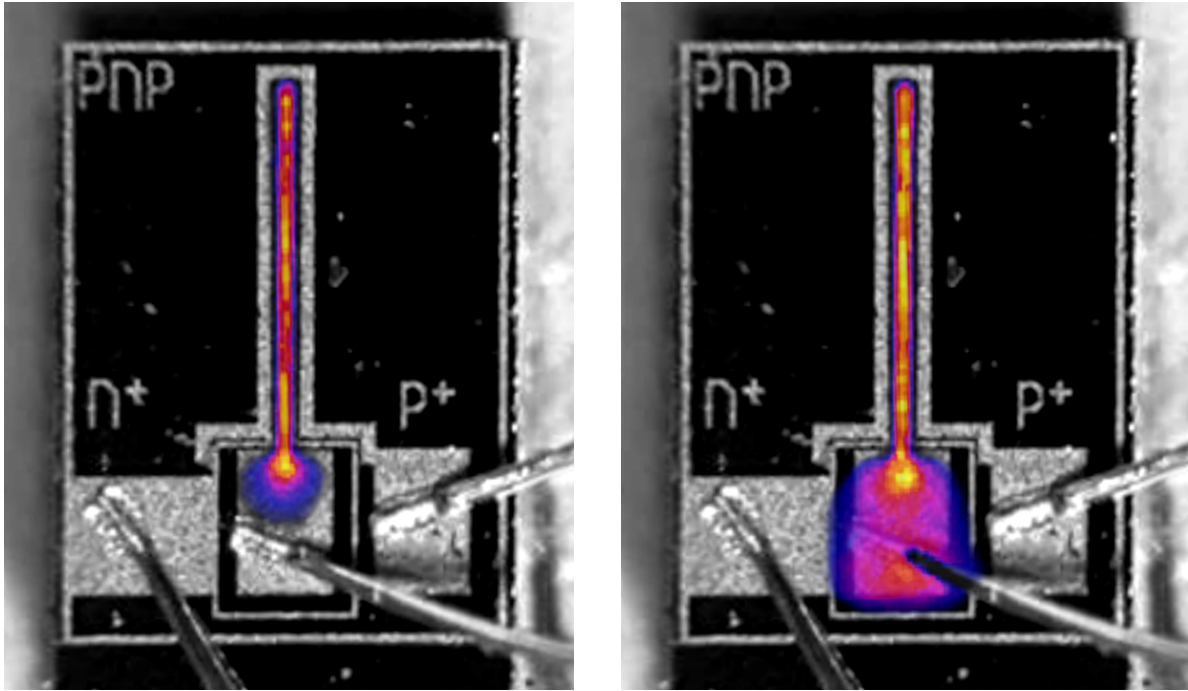
Figure 11. IBIC results for PNP detector with strip and guard ring biased at -2 V
(left) and with strip and guard ring biased at -10 V respectively. Results have been
over-layed on top of an optically zoomed microscopy image of the PNP detector

in Fig. 12, which depicts the guard ring at a variety of biases from 0 to -10 V. A slight
"bulging" in the charge collection is observed at the end of the strip, likely due to the
electric field distribution.

For each bias configuration, multiple line profiles in the x direction are taken across
the strip for different values of y. Each line profile is averaged to depict the charge
collection across the strip between the range 5µm $\leq$ y $\leq$ 25µm. Using the full width
half maximum as a figure of merit, the definition of the sensitive volume in terms of
width readily improves with increasing guard ring bias from 14 µm at 0V to 11 µm
at -10V. The result is suggestive that the spatial definition in face-on mode can be
optimised, with only minimal loss to the collected signal, see Fig. 12.

4.3. TCAD Modelling

The PNP device modelled using Synopsys TCAD simulation package (see Fig. 13). The
aim of the simulations was to model the electric field distribution of the device under
operating conditions. In all cases the bias voltage was applied to the strip contact and
guard ring (n+ blue lines in Fig. 13), whilst ground ring contact (p+ red lines in Fig.
13) were grounded.

Fig. 13, 14 and 15, depict the electric field distribution of the PNP device at 0, -2 and
-5 V respectively. The electric field distribution can be used to predict the width of
the SV. The results in passive mode, i.e. at 0 V (see Fig. 13), indicate the presence
of a built-in potential with the magnitude of the electric field in passive mode being
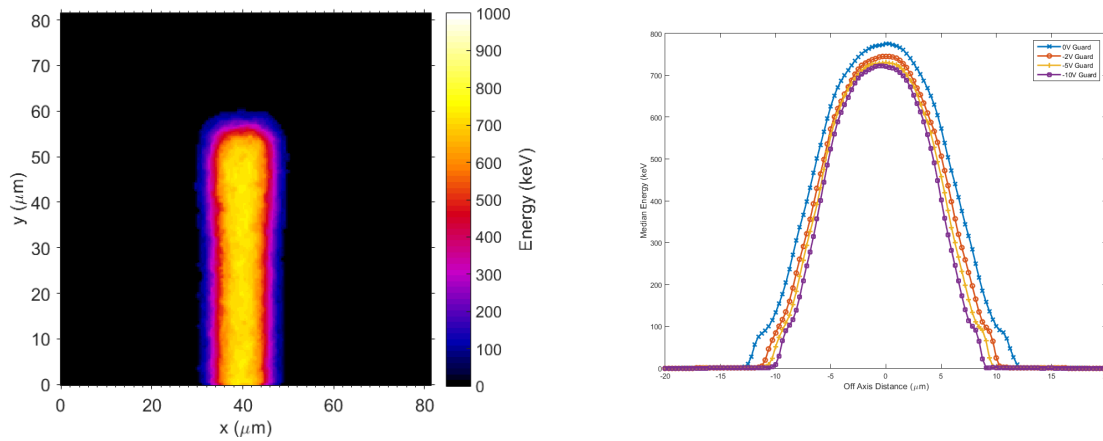
Figure 12. Left- Median energy map of PNP detector with strip at -2 V and Guard ring at -10 V. Right- Profile of the CCE across the strip at constant bias for varying guard ring bias between 0 and -10 V.

significantly higher around the ground ring than that of the strip or guard ring. Under operating conditions, i.e. -2 V (see Fig. 14), the width of the SV is closer to 10 to 15 µm. As the bias is increased to -5 V (see Fig. 15) and -10 V (see Fig. 16), the width continues to increase except where there is overlap with the field around the guard ring, which acts as a mechanism to restrict the electric field about the strip. The effect of the guard ring bias is further evidenced in Fig. 18, which depicts the electric field distribution taken across the PNP detector profile at 4 µm depth at a constant strip bias of -2 V and varying guard ring bias between 0 and -10 V. This profile is taken from the results previously described in Fig. 13 through 17. This models provides a means of determining the optimal bias configurations of the PNP detector.
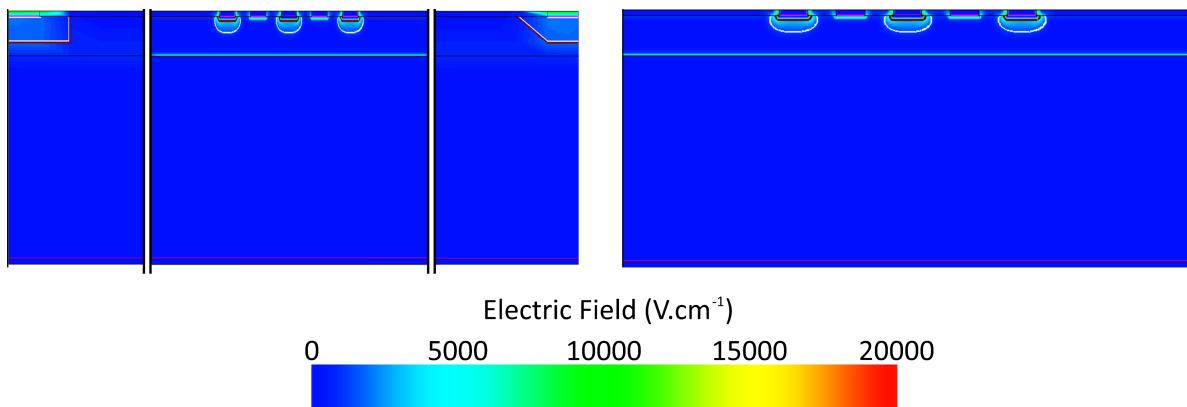

Figure 13. Left- 2D TCAD model of the PNP device as a cross-section through the strip. The vertical lines of either side of the PNP structure depict discontinuity breaks Right- Electric field distribution of the PNP device with strip at 0 V and guard ring biased at 0 V. The depletion region is indicated by the solid white line.

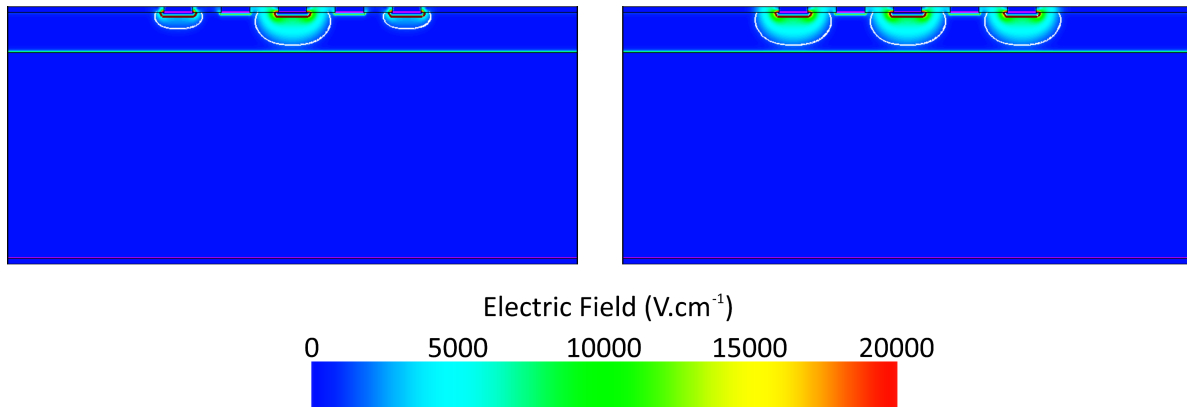The TCAD model provides a justification of the operating conditions for the PNP

Electric Field (V.cm⁻¹)

Figure 14. Left- Electric field distribution of the PNP device with strip at -2 V and guard ring biased at 0 V. Right- Electric field distribution of the PNP device with strip at -2 V and guard ring biased at -2 V. The depletion region is indicated by the solid white line.
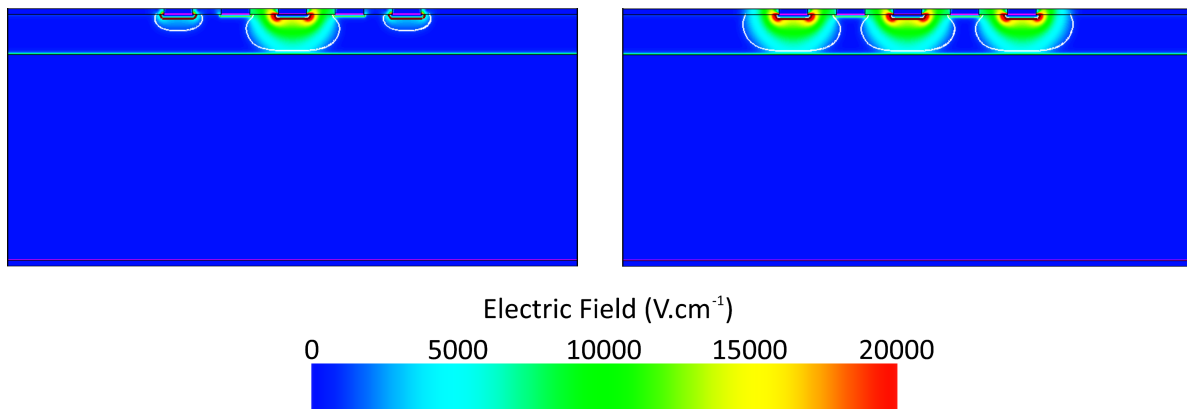

Electric Field (V.cm⁻¹)

Figure 15. Left- Electric field distribution of the PNP device with strip at -5 V and guard ring biased at 0 V. Right- Electric field distribution of the PNP device with strip at -5 V and guard ring biased at -5 V. The depletion region is indicated by the solid white line.

device and provides a suitable platform to estimate the spatial resolution of the device. The results derived from the 2D TCAD model of the PNP device agree well with the experimental results obtained using the IBIC experiment. The results of the TCAD model demonstrate the potential effectiveness of the detector architecture confining the electric field distribution to the designated volume given an appropriate choice of bias conditions.

4.4. Synchrotron Testing

4.4.1. Broad-beam field characterisation The signal from the PNP was calibrated with respect to a PTW PinPoint IC at 20 mm depth within a Gammex solid water phantom in broad-beam configuration, i.e. without MSC-induced spatial fractionation. The field size used in this experiment was 30 mm x 2.015 mm, as defined by the beam defining
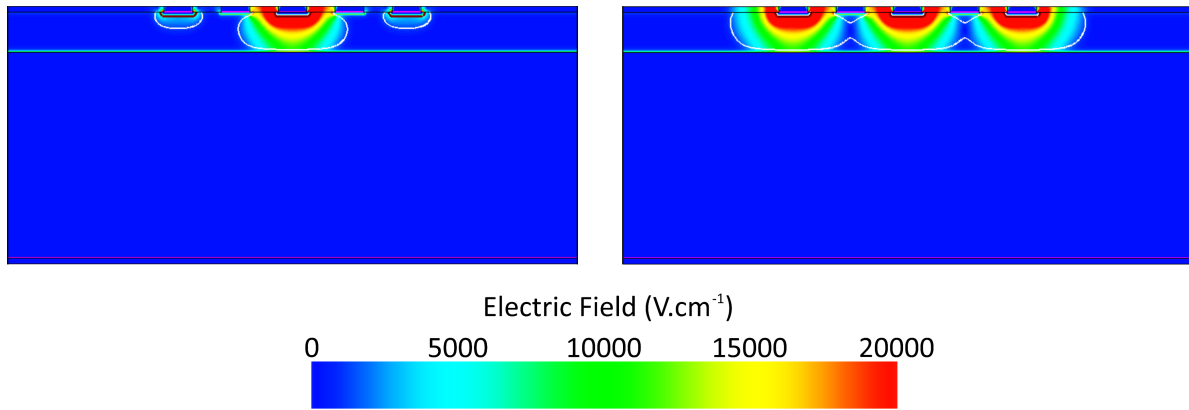
Figure 16. Left- Electric field distribution of the PNP device with strip at -10 V and guard ring biased at 0 V. Right- Electric field distribution of the PNP device with strip at -10 V and guard ring biased at -10 V. The depletion region is indicated by the solid white line.
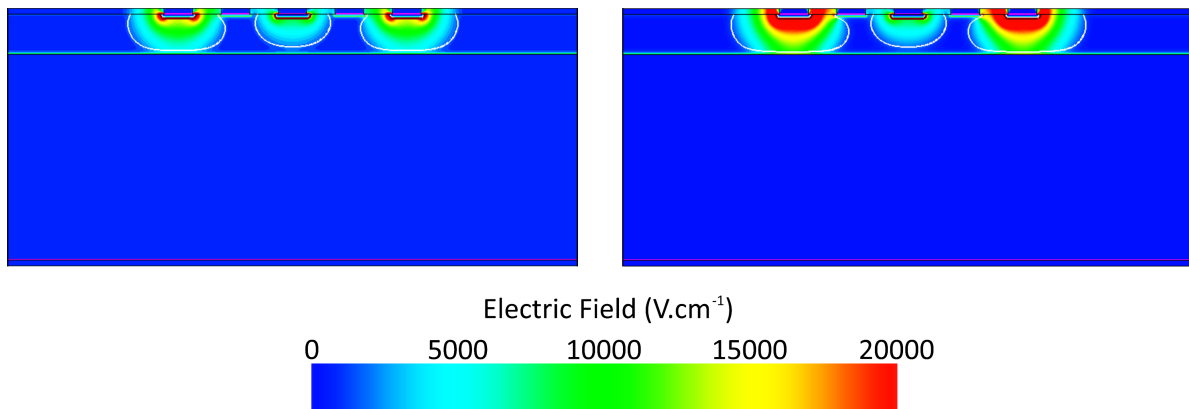

Figure 17. Electric field distribution of the PNP device with strip at constant bias of -2 V and guard ring biased at -5 V (left) and -10 V (right).

aperture. The results of the broad beam study were used to determine a calibration factor (K with units $\mathrm{Gy\,C^{-1}}$) to convert ADC counts to dose. The PNP was scanned horizontally through the broad-beam field in order to characterise its shape at a given depth (20 mm). The results of this scan are presented in Fig. 19. The uniformity of the broad beam profile is consistent with those of alternative detectors/dosimeters tested within the context of synchrotron radiation sources. The width of the profile was measured to be approximately 36.5 mm with 12% roll off from the in-field to out of field which is in good agreement with the expected field size as defined by the collimator slits and beam defining apertures. The PNP was used to verify the experimental set-up in order to produce the desired homogeneous and symmetric broad-beam profile that would after insertion of the MSC produce well defined microbeams representative of MRT. The increased size of the broad-beam profile is hypothesised to be caused by some slight beam divergence.

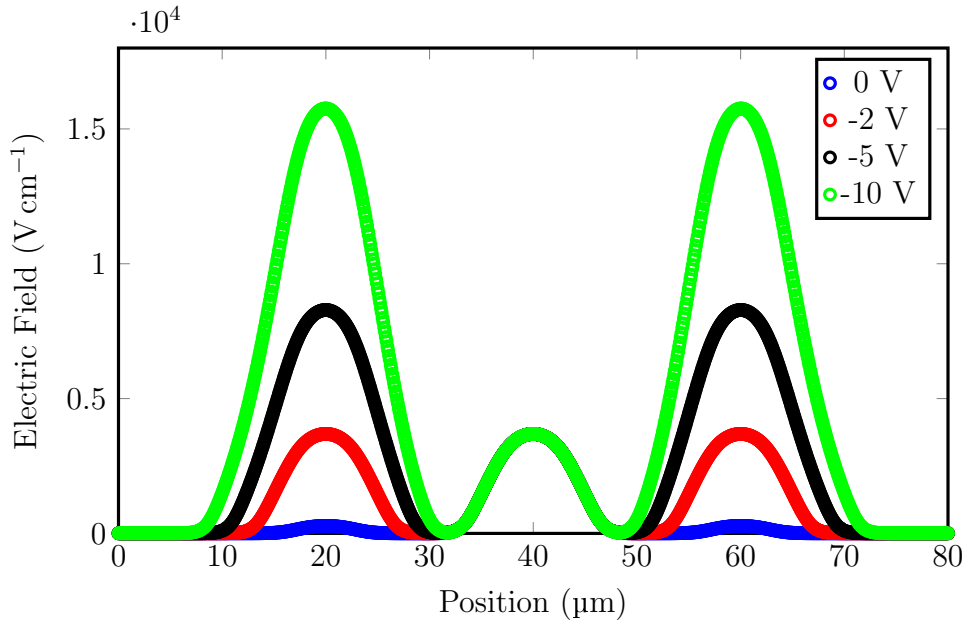Following the characterisation of the broad-beam field to ensure uniformity, ex-

Figure 18. Line profiles of the electric field distribution taken horizontally across the modelled cross section at 4 µm depth. The strip is biased at -2 V and the guard ring is biased at 0 (blue), -2 (red), -5 (black) and -10 V (green).

vacuo filtration was inserted (see Table 1). The PNP device was exposed to the broad-beam field in edge-on mode for different lengths of time from 50 ms up to 8000 ms. The integral counts as measured by the detector for each interval of irradiation time was converted to dose using the predetermined correction factor. The dose (Gy) as a function of irradiation time is depicted in Fig. 20. The PNP device demonstrates dose linearity within the range tested, with a total accumulated dose over the entire radiation procedure equal to 3 kGy demonstrating the reproducibility of dose measurements.

4.4.2. Collimator Rotation Study A collimator rotation study was performed prior to the characterisation of the microbeam radiation field. The purpose of this study was to ensure that the MSC is appropriate aligned with respect to the beam. The MSC was aligned by monitoring the output of the PNP detector as it was scanned at a constant speed of 2 mm s^{-1} at 20 mm depth in a solid water phantom through the microbeam field whilst rotating the MSC about the vertical axis perpendicular to beam direction. The MSC was rotated through small angles, ranging from -0.4° to 0.4° in increments of 0.1°. The microbeam profiles for each MSC angle between -0.1° to 0.1° are presented in Fig. 21 and 22 compared to ensure the best alignment of the MSC, i.e. MSC angle of 0°. In this study, the angle for which the MSC is best aligned is defined as $\theta_{aligned} = 0°$. No ev-vacuo filtration was used in this portion of the experiment.

4.4.3. Microbeam field characterisation The performance of the PNP device was evaluated within the microbeam configuration. The PNP was used to measure the
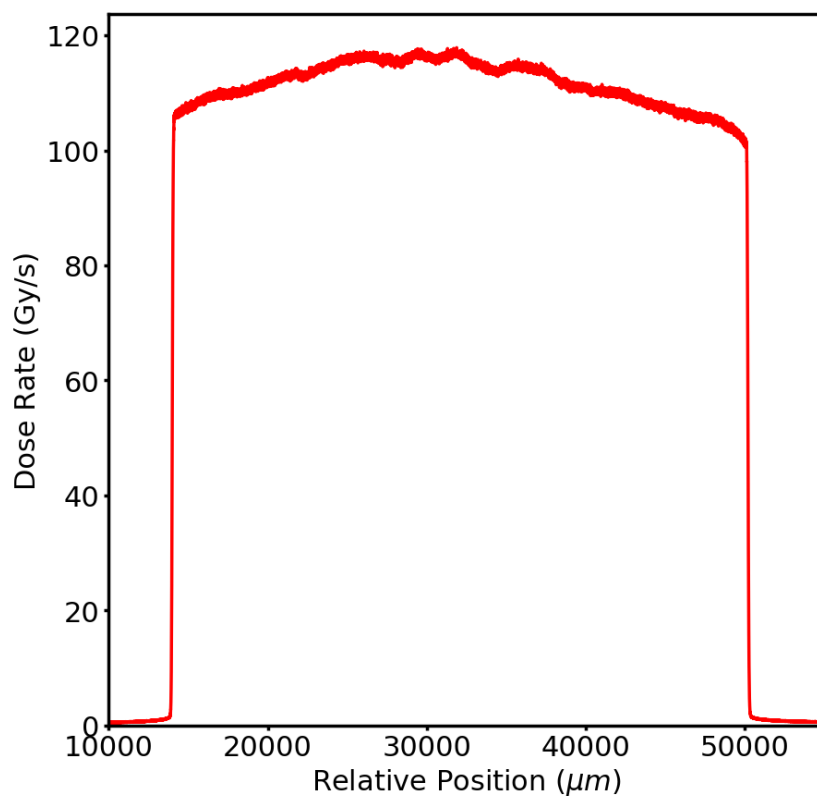
Figure 19. PNP detector in edge-on mode in broad-beam field. The roll-off of the field is clearly depicted.
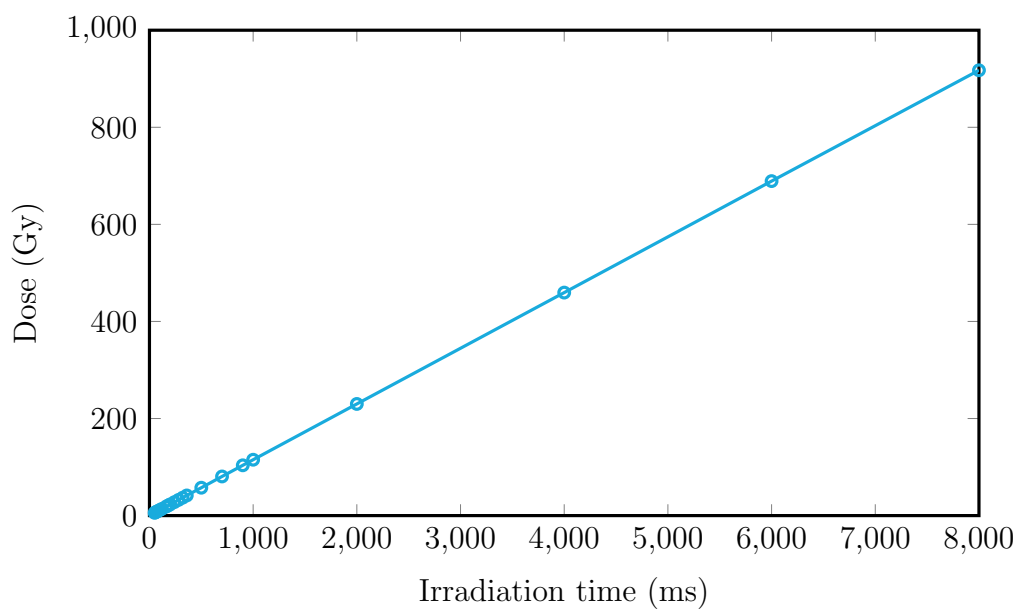

Figure 20. Dose Linearity of the PNP detector

microbeam field profile in both edge-on and face-on modes, with and without ex-vacuo filters in hutch 2A (see Table 1). From previous IBIC and TCAD based studies, the
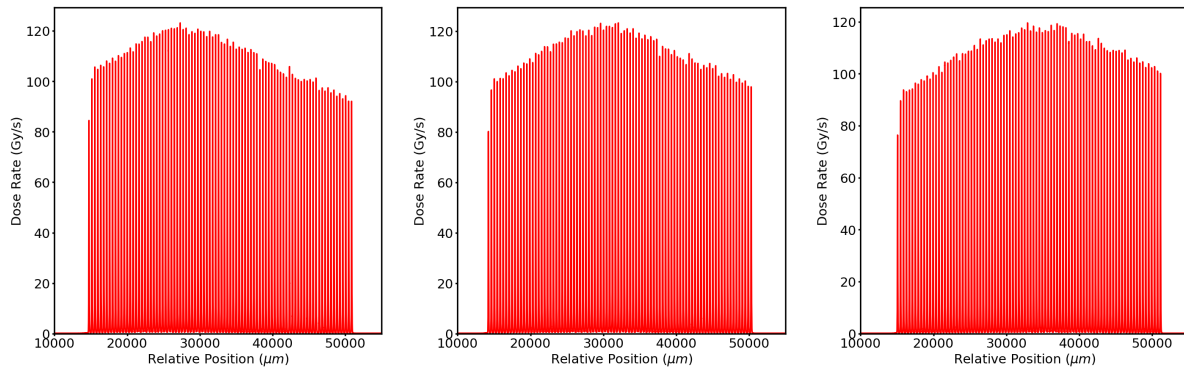
Figure 21. Microbeam profile for MSC at angle: -0.1° (left), 0° (middle) and 0.1° (right).
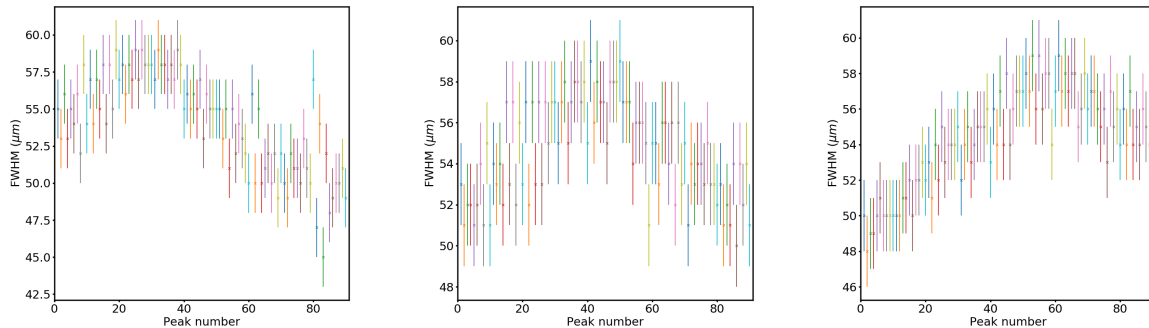

Figure 22. FWHM for each microbeam for MSC at angle: -0.1° (left), 0° (middle) and 0.1° (right). Vertical error bars are depicted to one standard deviation.

spatial resolution of the device is approximately of 15 µm. Thus given appropriate alignment with the incident microbeams, the PNP should hypothetically be well suited to measuring parameters of interest for MRT, i.e. FWHM, PVDR and Peak to peak distance.

The Gammex phantom with embedded PNP detector was scanned through the microbeam at a constant speed of 2 mm s^{-1}. Fig. 23 depicts the full microbeam profile obtained with the SSD at 20 mm depth in edge-on (left) and face-on mode (right) with ex-vaccuo filtration added, with 90 microbeams clearly resolved. A subset of the microbeams is depicted in Fig. 24 in addition to FWHM and PVDR for the entire profile measured, respectively, in edge-on mode. The experiment was then repeated with the detector in face-on mode. The full microbeam profile is presented in Fig. 25, with microbeam subset, microbeam FWHMs and PVDRs, respectively. The average FWHM, PVDR and peak-to-peak distance for both edge on and face on modes are presented in Table 2. All uncertainties listed are one standard deviation.

The data acquired using the X-Tream dosimetry system [9] was passed through a custom analysis script written in python to plot microbeam profiles and the FWHM and PVDR for each measured microbeam. These plots were used to extract the average FWHM, PVDR and peak to peak distance along with the associated experimental
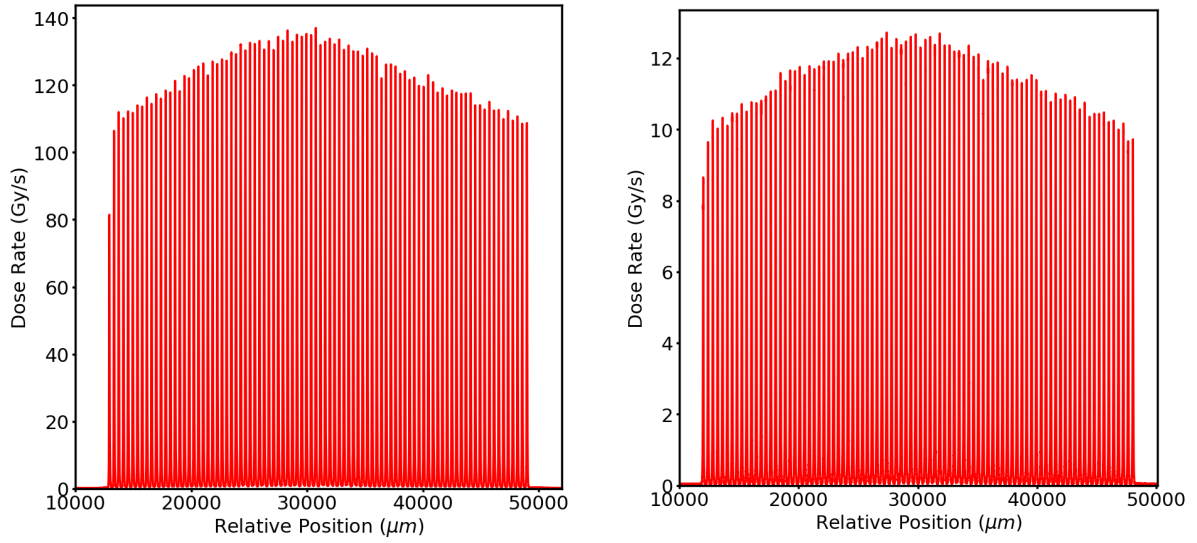
Figure 23. Full microbeam profile using PNP detector in edge-on mode (left) and face-on mode (right) with ex-vacuo filtration.
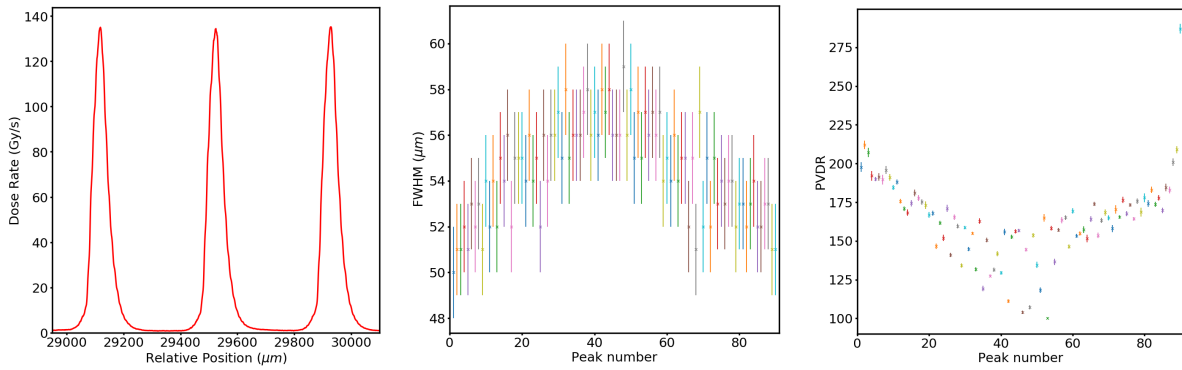

Figure 24. PNP detector in edge-on mode with ex-vacuo filtration, see Table 1. Subset of the Microbeam profile (left), FWHM (middle) and PVDR (right).
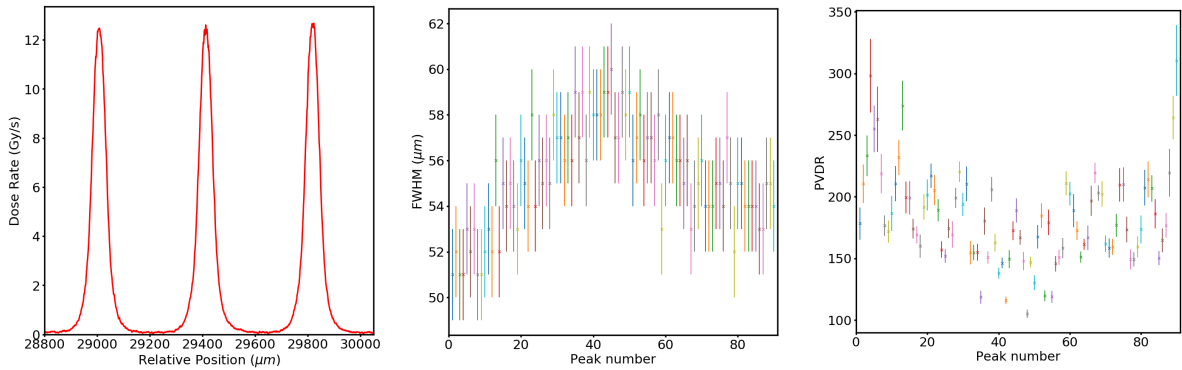

Figure 25. PNP detector in face-on mode with ex-vacuo filtration, see Table 1. Subset of the Microbeam profile (left), FWHM (middle) and PVDR (right).

uncertainty. As previously mentioned, the physical dimensions for each 'slot' in the MSC is 50 μm and has a centre to centre spacing or pitch of 400 μm. The FWHM is a

Mode	Parameter	Value
Edge-On	Mean FWHM	54.46 ± 2.08 µm
Face-On	Mean FWHM	55.31 ± 2.22 µm
Edge-On	Mean PVDR	163.95 ± 26.19
Face-On	Mean PVDR	182.98 ± 37.83
Edge-On	Mean Peak-to-Peak Distance	405.03 ± 2.59 µm
Face-On	Mean Peak-to-Peak Distance	405.01 ± 3.13 µm
Both	Number of microbeams	90

Table 2. Microbeam results of PNP detector in edge-on and face-on modes. All measurements are derived from experiments with no ex-vacuo filtration in Hutch 2A (see Table 1)

convolution of the PNPs point spread function (intrinsic spatial resolution), microbeam divergence and PNP misalignment. While not within experimental uncertainty, the determination of the FWHM is in reasonable agreement to the expected result of 50 µm. Likewise the PVDR, whilst arguably high is also quite reasonable given that similar results have been observed in the literature [9]. It should be noted that any inaccuracies within the measurement of the FWHM will also have a corresponding impact upon the accuracy of the PVDR, i.e. an increase in the measured FWHM results in a corresponding decrease in PVDR of the measured microbeams in both edge-on and face-on orientations.

5. Discussions and Conclusions

In this study, a new silicon strip detector design (PNP) was experimentally characterised by means of electrical (Current-Voltage and Capacitance-Voltage) and IBIC (Ion Beam Induced Charge) measurements to test functionality for application in Microbeam Radiation Therapy. The electrical characterisation indicates that the device will have low leakage current (< 0.001 nA) under operating bias conditions, i.e -2 V, with built-in potential and doping concentrations of 0.43 V and 4.1 $\times 10^{15}$ cm^{-3}, respectively. Ion Beam Induced Charge measurements have demonstrated that the CCE associated with the generation of free carriers following ionization in SV by a traversing projectile is confined to the desired sensitive volume (SV) region provided that the guard ring is appropriately biased. The maximum CCE within the PNP device was approximately 81% confirming the high quality of the device and silicon material used. Additionally it is observed that the spatial resolution of face-on mode operation can be optimised via guard ring bias technique from 15 to 11 µm without changes to the device architecture. The IBIC study has shown that the depth of collection region is approximately 5 µm, indicating edge-on mode to have an improved spatial resolution as compared to its face-on mode counterpart.

Measurements of highly intense X-rays in both broad-beam (BB) and microbeam (MB)

configurations were performed using the PNP device at the Australian Synchrotron (AS). The PNP device was used to characterise the BB and MB fields. Additionally, the PNP device was used to measure the full width at half maximum (FWHM) and peak to valley dose ratio (PVDR) of MBs having peak widths of 50 µm with pitch of 400 µm. In edge-on mode, the PNP device, was able to determine the average full width half maximum and peak to valley dose ratio across 90 microbeams to be 54 ± 2 µm and 164 ± 26. Similarly, in face-on mode, the PNP device, was able to determine the average full width half maximum and peak to valley dose ratio across 90 microbeams to be 55 ± 2 µm and 183 ± 38. Results in Face-on mode for this experiment were hampered by performing the experiment with the guard ring left floating, resulting in an increased SV. However, regardless of orientation, i.e. edge-on or face-on, the PNP device performed well with only a slight over-estimation of the FWHM. Face-on mode operation is currently limited by the state of fabrication techniques. Until the fabrication of strips with width less than 10 µm are readily reproducible and cost effective, edge-on mode operation clearly provides the best results for synchrotron generated microbeam profiling in terms of spatial resolution. This is supported by both IBIC and synchrotron based measurements. During the experimental measurements at the AS, the device was observed to have an excellent dose linearity up to 1000 Gy per exposure. Whilst the radiation hardness of the device was sufficient, the use of p-type as opposed to n-type silicon will undoubtedly improve this quality.

The results presented are promising and provide further support for the use of silicon strip detectors technologies for quality assurance of microbeam radiation therapy. Measurement accuracy can be improved by performing measurements with the guard ring biased. A new X-Tream data acquisition system has been commissioned to allow for measurements to be performed for multiple detector configurations including the option of biasing the guard ring. Future work concerning the PNP detector will focus upon improving measurement protocols in order to test the upper limits of the PNP detectors ability to accurately measure synchrotron generated microbeams. Future p-type devices will incorporate p-stop technology underneath the contact electrodes to limit collection underneath the pad, allowing for high resolution measurements at high bias operation.

6. Acknowledgements

References

[1] D. N. Slatkin, P. Spanne, F. A. Dilmanian, M. Sandborg, Microbeam radiation therapy, Medical Physics 19 (39) (1992) 1395–1234. doi:10.1118/1.3681274.
URL http://dx.doi.org/10.1118/1.596771{%}5Cnhttp://scitation.aip.org/content/aapm/journal/medphys/19/6?ver=pdfcov

[2] J. C. Crosbie, R. L. Anderson, K. Rothkamm, C. M. Restall, L. Cann, S. Ruwanpura, S. Meachem, N. Yagi, I. Svalbe, R. A. Lewis, B. R. G. Williams, P. A. W. Rogers, Tumor cell response to synchrotron microbeam radiation therapy differs markedly from cells in normal tissues., International journal of radiation oncology, biology, physics 77 (3) (2010) 886–94. doi:10.1016/j.ijrobp.2010.01.035.
URL http://www.ncbi.nlm.nih.gov/pubmed/20510199

[3] J. A. Laissue, G. Geiser, P. O. Spanne, F. A. Dilmanian, J. O. Gebbers, M. Geiser, X. Y. Wu, M. S. Makar, P. L. Mica, M. M. Nawrocky, D. D. Joel, D. N. Slatkin, Neuropathology of ablation of rat gliosarcomas and contiguous brain tissues using a microplanar beam of synchrotron-wiggler-generated X rays, International Journal of Cancer 78 (5) (1998) 654–660. doi:10.1002/(SICI)1097-0215(19981123)78:5<654::AID-IJC21>3.0.CO;2-L.

[4] A. Bouchet, B. Lemasson, G. Le Duc, C. Maisin, E. Bräuer-Krisch, E. A. Siegbahn, L. Renaud, E. Khalil, C. Rémy, C. Poillot, A. Bravin, J. A. Laissue, E. L. Barbier, R. Serduc, Preferential Effect of Synchrotron Microbeam Radiation Therapy on Intracerebral 9L Gliosarcoma Vascular Networks, International Journal of Radiation Oncology*Biology*Physics 78 (5) (2010) 1503–1512. doi:10.1016/j.ijrobp.2010.06.021.
URL http://linkinghub.elsevier.com/retrieve/pii/S0360301610008709

[5] F. A. Dilmanian, T. M. Button, G. L. Duc, N. Zhong, A. Louis, J. A. L. Smith, S. R. Martinez, T. Bacarian, J. Tammam, B. Ren, P. M. Farmer, J. Kalef-ezra, P. L. Micca, M. M. Nawrocky, J. A. Niederer, F. P. Recksiek, A. Fuchs, E. M. Rosen, F. A. D. Ny, Response of 9LGS to microbeam radiation, Neuro-Oncology (2002) 26–38.

[6] P. Regnard, G. L. Duc, E. Bräuer-Krisch, I. Troprès, E. A. Siegbahn, A. Kusak, C. Clair, H. Bernard, D. Dallery, J. A. Laissue, A. Bravin, Irradiation of intracerebral 9L gliosarcoma by a single array of microplanar x-ray beams from a synchrotron: balance between curing and sparing, Physics in Medicine and Biology 53 (4) (2008) 861–878. doi:10.1088/0031-9155/53/4/003.
URL http://stacks.iop.org/0031-9155/53/i=4/a=003?key=crossref.0387b3f4eac8378fe73c877e361c2b20

[7] A. W. Stevenson, J. C. Crosbie, C. J. Hall, J. Livingstone, J. E. Lye, Quantitative characterisation of the X-ray beam at the Australian Synchrotron Imaging and Medical Beamline (IMBL)*, Journal of Synchrotron Radiation.

[8] E. Brauer-Krisch, A. Bravin, M. Lerch, A. Rosenfeld, J. Stepanek, M. Di Michiel, J. A. Laissue, MOSFET dosimetry for microbeam radiation therapy at the European Synchrotron Radiation Facility, Medical Physics 30 (4) (2003) 583. doi:10.1118/1.1562169.
URL http://scitation.aip.org/content/aapm/journal/medphys/30/4/10.1118/1.1562169

[9] M. Petasecca, A. Cullen, I. Fuduli, A. Espinoza, C. Porumb, C. Stanton, A. H. Aldosari, E. Bräuer-Krisch, H. Requardt, A. Bravin, V. Perevertaylo, A. B. Rosenfeld, M. L. F. Lerch, X-Tream: a novel dosimetry system for Synchrotron Microbeam Radiation Therapy, Journal of Instrumentation 7 (07). doi:10.1088/1748-0221/7/07/P07022.
URL http://stacks.iop.org/1748-0221/7/i=07/a=P07022?key=crossref.8d1255d7745abc72cb917ba74e51af5f

[10] EBT3- Gafchromic Film.
URL http://www.gafchromic.com/

[11] S. Vahedi, G. Okada, B. Morrell, E. Muzar, C. Koughia, A. Edgar, C. Varoy, G. Belev, T. Wysokinski, D. Chapman, S. Kasap, X-ray induced Sm 3+ to Sm 2+ conversion in

fluorophosphate and fluoroaluminate glasses for the monitoring of high-doses in microbeam radiation therapy, Journal of Applied Physics 112 (7) (2012) 073108. doi:10.1063/1.4754564.
URL http://aip.scitation.org/doi/10.1063/1.4754564

[12] G. Okada, J. Ueda, S. Tanabe, G. Belev, T. Wysokinski, D. Chapman, D. Tonchev, S. Kasap, Samarium-doped oxyfluoride glass-ceramic as a new fast erasable dosimetric detector material for microbeam radiation cancer therapy applications at the canadian synchrotron, Journal of the American Ceramic Society 97 (7) (2014) 2147–2153. doi:10.1111/jace.12938.

[13] PTW.
URL http://www.ptw.de/2253.html

[14] J. Livingstone, A. W. Stevenson, D. J. Butler, D. Häusermann, J.-f. Adam, Characterization of a synthetic single crystal diamond detector for dosimetry in spatially fractionated synchrotron x-ray fields, Medical Physics 43 (7) (2016) 4283–4293. doi:10.1118/1.4953833.
URL http://dx.doi.org/10.1118/1.4953833http://scitation.aip.org/content/aapm/journal/medphys/43/7/10.1118/1.4953833http://dx.doi.org/10.1118/1.4953833{%}5Cnhttp://scitation.aip.org/content/aapm/journal/medphys/43/7/10.1118/1.4953833

[15] P. Fournier, I. Cornelius, A. Dipuglia, M. Cameron, J. A. Davis, A. Cullen, M. Petasecca, A. B. Rosenfeld, E. Bräuer-Krisch, D. Häusermann, A. W. Stevenson, V. Perevertaylo, M. L. Lerch, X-Tream dosimetry of highly brilliant X-ray microbeams in the MRT hutch of the Australian Synchrotron, Radiation Measurements (2017) 1–7doi:10.1016/j.radmeas.2017.01.011.
URL http://linkinghub.elsevier.com/retrieve/pii/S135044871730046X

[16] A. Rosenfeld, G. Kaplan, T. Kron, B. Allen, A. Dilmanian, I. Orion, B. Ren, M. Lerch, A. Holmes-Siedle, MOSFET dosimetry of an X-ray microbeam, IEEE Transactions on Nuclear Science 46 (6) (1999) 1774–1780. doi:10.1109/23.819153.
URL http://ieeexplore.ieee.org/lpdocs/epic03/wrapper.htm?arnumber=819153

[17] A. Rosenfeld, E. Siegbah, E. Brauer-Krish, A. Holmes-Siedle, M. Lerch, A. Bravin, I. Cornelius, G. Takacs, N. Painuly, H. Nettelback, T. Kron, Edge-on face-to-face MOSFET for synchrotron microbeam dosimetry: MC modeling, IEEE Transactions on Nuclear Science 52 (6) (2005) 2562–2569. doi:10.1109/TNS.2005.860704.
URL http://ieeexplore.ieee.org/document/1589239/

[18] M. Lerch, M. Petasecca, A. Cullen, A. Hamad, H. Requardt, E. Bräuer-Krisch, A. Bravin, V. Perevertaylo, A. Rosenfeld, Dosimetry of intensive synchrotron microbeams, Radiation Measurements 46 (12) (2011) 1560–1565. doi:10.1016/j.radmeas.2011.08.009.
URL http://dx.doi.org/10.1016/j.radmeas.2011.08.009http://linkinghub.elsevier.com/retrieve/pii/S1350448711004215

[19] M. B. H. Breese, A theory of ion beam induced charge collection, Journal of Applied Physics 74 (6) (1993) 3789–3799. doi:10.1063/1.354471.

[20] E. Vittone, Z. Pastuovic, M. Breese, J. Garcia Lopez, M. Jaksic, J. Raisanen, R. Siegele, A. Simon, G. Vizkelethy, Charge collection efficiency degradation induced by MeV ions in semiconductor devices: Model and experiment, Nuclear Instruments and Methods in Physics Research Section B: Beam Interactions with Materials and Atoms 372 (2016) 128–142. doi:10.1016/j.nimb.2016.01.030.
URL http://dx.doi.org/10.1016/j.nimb.2016.01.030http://linkinghub.elsevier.com/retrieve/pii/S0168583X16000872

[21] Z. Pastuovic, R. Siegele, D. Cohen, M. Mann, M. Ionescu, D. Button, S. Long, The new confocal heavy ion microprobe beamline at ANSTO: The first microprobe resolution tests and applications for elemental imaging and analysis, Nuclear Instruments and Methods in Physics Research Section B: Beam Interactions with Materials and Atoms 404 (2017) 1–8. doi:10.1016/j.nimb.2017.01.059.
URL http://linkinghub.elsevier.com/retrieve/pii/S0168583X17300745

[22] J. F. Ziegler, M. D. Ziegler, J. P. Biersack, SRIM - The stopping and range of ions in matter

(2010), Nuclear Instruments and Methods in Physics Research, Section B: Beam Interactions with Materials and Atoms 268 (11-12) (2010) 1818–1823. `doi:10.1016/j.nimb.2010.02.091`.
URL `http://dx.doi.org/10.1016/j.nimb.2010.02.091`

[23] Synopsys TCAD (2013).
URL `http://www.synopsys.com/Tools/TCAD`

[24] M. Cameron, I. Cornelius, D. Cutajar, J. Davis, A. Rosenfeld, M. Lerch, S. Guatelli, Comparison of phantom materials for use in quality assurance of microbeam radiation therapy, Journal of Synchrotron Radiation 24 (4). `doi:10.1107/S1600577517005641`.
URL `http://scripts.iucr.org/cgi-bin/paper?S1600577517005641`